

Parabolic Encounters

C. P. L. Berry^{1*} and J. R. Gair¹

¹*Institute of Astronomy, University of Cambridge, Madingley Road, Cambridge, CB3 0HA*

6 May 2011

ABSTRACT

I thought I would try out the MNRAS \LaTeX style.

Key words: black hole physics – Galaxy: centre – gravitational waves – methods: data analysis.

1 BACKGROUND AND INTRODUCTION

Many, if not all, galactic nuclei are believed to have harboured a massive black hole (MBH) during their evolution (Lynden-Bell & Rees 1971; Rees 1984). The best opportunity to study these objects comes from the compact object in our own galactic centre (GC), which is coincident with Sagittarius A* (Sgr A*). This is identified as an MBH of mass $M_{\bullet} = 4.31 \times 10^6 M_{\odot}$ at a distance of only $R_0 = 8.33$ kpc (Gillessen et al. 2009). According to the no-hair theorem, the MBH should be described completely by its mass M_{\bullet} and spin a , since we expect the charge of an astrophysical black hole to be negligible (Israel 1967, 1968; Carter 1971; Hawking 1972; Robinson 1975; Chandrasekhar 1998). Consequently, to gain a full understanding of the MBH we need to measure its spin. This will give us insight into its history and role in the evolution of the Galaxy.

It has been suggested that the spin could be inferred from careful observation of the orbits of stars within a few milliparsec of the GC (Merritt et al. 2010), although this is complicated because of perturbations due to other stars, or from observations of quasi-periodic oscillations (QPOs) of radio emissions (Kato et al. 2010), though there are difficulties in interpreting these results (Psaltis 2008).

This latter method has produced a value of the dimensionless spin, $a_* = Jc/GM_{\bullet}^2$ where J is the MBH's angular momentum, of $a_* = 0.44 \pm 0.08$. To obtain this result Kato et al. (2010) have combined their observations of Sgr A* with observations of galactic X-ray sources containing solar mass BHs, to find a best-fit unique spin parameter for all BHs. However, it is not clear that all BHs should share the same value of the spin parameter; especially considering that the BHs considered here differ by six orders of magnitude, with none in the intermediate range. Even if BH spin is determined by a universal process, we would expect some distribution of spin parameters (King et al. 2008). Thus we cannot precisely determine the spin of the galactic centre's MBH from an average including other BHs.

While we can use the spin of other BHs as a prior, to inform us of what we should expect to measure for the MBH's spin, it is desirable to have an independent measurement.

An exciting means of inferring information about the MBH is through gravitational waves (GWs) emitted when compact objects (COs), such as smaller black holes (BHs), neutron stars (NSs), white dwarfs (WDs) or low mass main sequence (MS) stars, pass close by. The proposed Laser Interferometer Space Antenna (LISA) mission is designed to be able to detect GWs in the frequency range of interest for these encounters (Bender et al. 1998; Danzmann & Rüdiger 2003). The identification of waves requires a set of accurate waveform templates covering parameter space. Much work has already been done on the waveforms generated when companion objects inspiral towards an MBH; as they orbit, the GWs carry away energy and angular momentum, causing the orbit to shrink until eventually the object plunges into the MBH. The initial orbits may be highly elliptical and a burst of radiation is emitted during each close encounter. These are known as extreme mass-ratio bursts (EMRBs; Rubbo et al. 2006). Assuming that the companion is not scattered from its orbit, and does not plunge straight into the MBH, its orbit will evolve, becoming more circular, and it will begin to continuously emit significant gravitational radiation in the LISA frequency range. The resulting signals are known as extreme mass-ratio inspirals (EMRIs) (Amaro-Seoane et al. 2007).

Studies of these systems have usually focused upon when the orbit completes multiple cycles, allowing a high signal-to-noise ratio to be accumulated. Here, we will investigate what can be learnt from high eccentricity orbits. These are the initial bursting orbits from which an EMRI may evolve. The event rate for the detection of such EMRBs with LISA has been estimated to be as high as 15 yr^{-1} (Rubbo et al. 2006), although this has been revised downwards to the order of 1 yr^{-1} (Hopman et al. 2007). Even if only a single burst is detected during the LISA mission, this is still an exciting possibility since the information carried by the GW should give an unparalleled probe of the structure of spacetime of the GC. Exactly what can be inferred will depend upon the orbit.

* E-mail: cplb2@cam.ac.uk

We will make the simplifying assumption that all these orbits are marginally bound, or parabolic, since highly eccentric orbits will appear almost indistinguishable from an appropriate parabolic orbit (Kobayashi et al. 2004). Here “parabolic” and “eccentricity” refer to the energy of the geodesic and not to the geometric shape of the orbit.¹ Following such a trajectory an object may make just one pass of the MBH or, if the periapsis distance is small enough, it may complete a number of rotations. Such an orbit is referred to as zoom-whirl (Glampedakis & Kennefick 2002).

In order to compute the gravitational waveform produced in such a case, we integrate the geodesic equations for a parabolic orbit in Kerr spacetime. We assume that the orbiting body is a test particle, such that it does not influence the underlying spacetime, and that the orbital parameters evolve negligibly during the orbit so that they may be held constant. We use this to construct an approximate numerical kludge waveform (Babak et al. 2007).

This paper is organised as follows. In Sec. 2 we discuss the construction of the geodesic orbits, and in Sec. 3 we explain how to construct a numerical kludge waveform from this trajectory. In Sec. 4 we establish what the LISA detectors would measure, in Sec. 5 how the signal would be analysed to extract the information encoded in the waveform. [Something else here] In Sec. 7 we confirm the accuracy of the kludge waveforms by comparing the energy flux with fluxes calculated from other approaches. We conclude in Sec. ?? with a summary of our results.

Throughout this work we will assume metric with signature $(+, -, -, -)$. Greek indices are used to represent space-time indices $\mu = \{0, 1, 2, 3\}$ and lowercase Latin indices from the middle of the alphabet are used for spatial indices $i = \{1, 2, 3\}$. Uppercase Latin indices from the beginning of the alphabet will be used for the output of two LISA detector-arms $A = \{I, II\}$, and lowercase Latin indices from the beginning of the alphabet are used for parameter space. Summation over repeated indices is assumed unless explicitly noted otherwise. Geometric units with $G = c = 1$ will be used where noted, but in general factors of G and c will be retained.

2 PARABOLIC ORBITS IN KERR SPACETIME

2.1 The metric and geodesic equations

Astrophysical BHs are described by the Kerr metric (Kerr 1963). In standard Boyer-Lindquist coordinates the line element is (Boyer & Lindquist 1967; Hobson et al. 2006, section 13.7)

$$ds^2 = \frac{\rho^2 \Delta}{\Sigma^2} c^2 dt^2 - \frac{\Sigma \sin^2 \theta}{\rho^2} (d\phi - \omega dt)^2 - \frac{\rho^2}{\Delta} dr^2 - \rho^2 d\theta^2, \quad (1)$$

¹ Marginally bound Keplerian orbits in flat spacetime are parabolic in both senses.

where we have introduced functions

$$\rho^2 = r^2 + a^2 \cos^2 \theta, \quad (2)$$

$$\Delta = r^2 - \frac{2GM_\bullet r}{c^2} + a^2, \quad (3)$$

$$\Sigma = (r^2 + a^2)^2 - a^2 \Delta \sin^2 \theta, \quad (4)$$

$$\omega = \frac{2GM_\bullet ar}{c\Sigma}. \quad (5)$$

The spin parameter a is related to the BH’s angular momentum by

$$J = M_\bullet ac. \quad (6)$$

For the remainder of this section we shall work in natural units with $G = c = 1$.

Geodesics are parameterized by three conserved quantities (aside from the particle’s mass μ): energy (per unit mass) E , specific angular momentum about the symmetry axis (the z -axis) L_z , and Carter constant Q (Carter 1968; Chandrasekhar 1998, section 62). The geodesic equations are

$$\rho^2 \frac{dt}{d\tau} = a (L_z - aE \sin^2 \theta) + \frac{r^2 + a^2}{\Delta} T, \quad (7)$$

$$\rho^2 \frac{dr}{d\tau} = \pm \sqrt{V_r}, \quad (8)$$

$$\rho^2 \frac{d\theta}{d\tau} = \pm \sqrt{V_\theta}, \quad (9)$$

$$\rho^2 \frac{d\phi}{d\tau} = \frac{L_z}{\sin^2 \theta} - aE + \frac{a}{\Delta} T, \quad (10)$$

where we have introduced potentials

$$T = E (r^2 + a^2) - aL_z, \quad (11)$$

$$V_r = T^2 - \Delta [r^2 + (L_z - aE)^2 + Q], \quad (12)$$

$$V_\theta = Q - \cos^2 \theta \left[a^2 (1 - E^2) + \frac{L_z^2}{\sin^2 \theta} \right], \quad (13)$$

and τ is proper time. The signs of the r and θ equations may be chosen independently.

For a parabolic orbit $E = 1$; the particle is at rest at infinity. This simplifies the geodesic equations. It also allows us to give a simple interpretation for Carter constant Q : this is defined as

$$Q = L_\theta^2 + \cos^2 \theta \left[a^2 (1 - E^2) + \frac{L_z^2}{\sin^2 \theta} \right], \quad (14)$$

where L_θ is the (non-conserved) specific angular momentum in the θ -direction ($V_\theta = L_\theta^2$). For $E = 1$ we have

$$Q = L_\theta^2 + \cot^2 \theta L_z^2 = L_\infty^2 - L_z^2, \quad (15)$$

where L_∞ is the total specific angular momentum at infinity, where the metric is asymptotically flat (de Felice 1980).² This is as in Schwarzschild spacetime.

2.2 Integration variables and turning points

In integrating the geodesic equations, difficulties can arise because of the presence of turning points in the motion, when the sign of the r or θ geodesic equation will change.

² See Rosquist et al. (2009) for a discussion of the interpretation of Q in the limit $G \rightarrow 0$, corresponding to a flat spacetime.

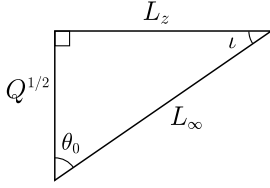


Figure 1. The angular momenta L_∞ , L_z and \sqrt{Q} define a right-angled triangle. The acute angles are θ_0 , the extremal value of the polar angle, and ι , the orbital inclination (Glampedakis & Kennefick 2002).

The radial turning points are at the periastris r_p and at infinity. We may locate the periastris by finding the roots of $V_r = 2M_\bullet r^3 - (L_z^2 + Q)r^2 + 2M_\bullet [(L_z - a)^2 + Q]r - a^2 Q = 0$. (16)

This has three roots, which we shall denote $\{r_1, r_2, r_p\}$; the periastris r_p is the largest real root. We do not find the apoapsis as a (fourth) root to this equation as we have removed it by taking $E = 1$ before solving; this turning point can be found by setting the unconstrained expression for V_r equal to zero, and then solving for $E(r)$; taking the limit $r \rightarrow \infty$ gives $E \rightarrow 1$ (Wilkins 1972).

We may avoid the difficulties of the turning point by introducing an angular variable that always increases with proper time (Drasco & Hughes 2004): inspired by Keplerian orbits, we parameterize our trajectory by

$$r = \frac{p}{1 + e \cos \psi}, \quad (17)$$

where $e = 1$ is the eccentricity and $p = 2r_p$ is the semilatus rectum. As ψ covers its full range from $-\pi$ to π , r traces out one full orbit from infinity through the periastris at $\psi = 0$ back to infinity. The geodesic equation for ψ is

$$\rho^2 \frac{d\psi}{d\tau} = \left\{ M_\bullet [2r_p - (r_1 + r_2)(1 + \cos \psi) + \frac{r_1 r_2}{2r_p} (1 + \cos \psi)^2] \right\}^{1/2}. \quad (18)$$

This may be integrated without problem. Parameterizing an orbit by its periastris and eccentricity has the additional benefit of allowing easier comparison with its flat-space equivalent (Gair et al. 2005).

The θ motion is usually bounded, with $\theta_0 \leq \theta \leq \pi - \theta_0$; in the event that $L_z = 0$ the particle follows a polar orbit and θ will cover its full range. The turning points are given by

$$V_\theta = Q - \cot^2 \theta L_z^2 = 0 \quad (19)$$

Only if $L_z = 0$ may we reach the poles (Wilkins 1972). If we change variable to $\zeta = \cos^2 \theta$, we have a maximum value $\zeta_0 = \cos^2 \theta_0$ given by

$$\zeta_0 = \frac{Q}{Q + L_z^2} = \frac{Q}{L_\infty^2}. \quad (20)$$

See Fig. 1 for a geometrical visualization. Let us now introduce a second angular variable (Drasco & Hughes 2004)

$$\zeta = \zeta_0 \cos^2 \chi. \quad (21)$$

Over one 2π period of χ , θ oscillates over its full range, from

its minimum value to its maximum and back. The geodesic equation for χ is

$$\rho^2 \frac{d\chi}{d\tau} = \sqrt{Q + L_z^2}, \quad (22)$$

and may be integrated simply.

3 WAVEFORM CONSTRUCTION

For given angular momenta L_z and Q , and initial starting position, we can calculate the geodesic trajectory. The orbiting body is assumed to follow this track exactly: we ignore evolution due to the radiation of energy and angular momentum, which should be negligible for EMRBs. From this trajectory we calculate the waveform using a semirelativistic approximation (Ruffini & Sasaki 1981): we assume that the particle moves along a geodesic in the Kerr geometry, but radiates as if it were in flat spacetime. This quick-and-dirty technique is known as a numerical kludge (NK), and has been shown to approximate well results computed by more accurate methods (Babak et al. 2007).

3.1 Kludge approximation

Numerical kludge approximations aim to encapsulate the main characteristics of a waveform by using the exact particle trajectory (ignoring inaccuracies from radiative effects and from the particles self-force), whilst saving on computational time by using approximate waveform generation techniques.

To start, we build an equivalent flat-space trajectory from the Kerr geodesic. This is done by identifying the Boyer-Lindquist coordinates with a set of flat-space coordinates; we consider two choices here:

(i) Identify the Boyer-Lindquist coordinates with flat-space spherical polars $\{r_{\text{BL}}, \theta_{\text{BL}}, \phi_{\text{BL}}\} \rightarrow \{r_{\text{sph}}, \theta_{\text{sph}}, \phi_{\text{sph}}\}$, then define flat-space Cartesian coordinates (Gair et al. 2005; Babak et al. 2007)

$$\mathbf{x} = \begin{pmatrix} r_{\text{sph}} \sin \theta_{\text{sph}} \cos \phi_{\text{sph}} \\ r_{\text{sph}} \sin \theta_{\text{sph}} \sin \phi_{\text{sph}} \\ r_{\text{sph}} \cos \theta_{\text{sph}} \end{pmatrix}. \quad (23)$$

(ii) Identify the Boyer-Lindquist coordinates with flat-space oblate-spheroidal coordinates $\{r_{\text{BL}}, \theta_{\text{BL}}, \phi_{\text{BL}}\} \rightarrow \{r_{\text{ob}}, \theta_{\text{ob}}, \phi_{\text{ob}}\}$ so that the flat-space Cartesian coordinates are

$$\mathbf{x} = \begin{pmatrix} \sqrt{r_{\text{ob}}^2 + a^2} \sin \theta_{\text{ob}} \cos \phi_{\text{ob}} \\ \sqrt{r_{\text{ob}}^2 + a^2} \sin \theta_{\text{ob}} \sin \phi_{\text{ob}} \\ r_{\text{ob}} \cos \theta_{\text{ob}} \end{pmatrix}. \quad (24)$$

These are appealing because in the limit that $G \rightarrow 0$, so that the gravitating mass goes to zero, the Kerr metric in Boyer-Lindquist coordinates reduces to the Minkowski metric in oblate-spheroidal coordinates.

In the limit of $a \rightarrow 0$, the two coincide, as they do in the limit of large r_{BL} .

It must be stressed that there is no well motivated argument that either coordinate system must yield an accurate GW; their use is justified *post facto* by comparison with results obtained from more accurate, and computationally intensive, methods (Gair et al. 2005; Babak et al. 2007).

The ambiguity in assigning flat-space coordinates reflects the inconsistency of the semi-relativistic approximation: the geodesic trajectory was calculated for the Kerr geometry; by moving to flat spacetime we lose the reason for its existence. However, this inconsistency should not be regarded as a major problem; it is just an artifact of the basic assumption that the shape of the trajectory is important for determining the character of the radiation, but the curvature of the spacetime in the vicinity of the source is not. By binding the particle to the exact geodesic, we ensure that the kludge waveform has spectral components at the correct frequencies, but by assuming flat spacetime for generation of GWs they will not have the correct amplitudes.

3.2 Quadrupole-octopole formula

Now we have a flat-space particle trajectory $x_p^\mu(\tau)$, we may apply a flat-space wave generation formula. We shall use the quadrupole-octopole formula to calculate the gravitational strain (Bekenstein 1973; Press 1977)

$$h^{jk}(t, \mathbf{x}) = -\frac{2G}{c^6 r} \left(\ddot{I}^{jk} - 2n_i \ddot{S}^{ijk} + n_i \ddot{M}^{ijk} \right)_{t'=t-r/c} \quad (25)$$

where an over-dot represents differentiation with respect to time t (and not τ), t' is the retarded time, $r = |\mathbf{x} - \mathbf{x}_p|$ is the radial distance, \mathbf{n} is the radial unit vector, and the mass quadrupole I^{jk} , current quadrupole S^{ijk} and mass octopole M^{ijk} are defined by

$$I^{jk}(t') = \int x'^j x'^k T^{00}(t', \mathbf{x}') d^3 x'; \quad (26)$$

$$S^{ijk}(t') = \int x'^j x'^k T^{0i}(t', \mathbf{x}') d^3 x'; \quad (27)$$

$$M^{ijk}(t') = \frac{1}{c} \int x'^i x'^j x'^k T^{00}(t', \mathbf{x}') d^3 x'. \quad (28)$$

This is correct for a slow moving source. It is the familiar quadrupole formula (Misner et al. 1973, section 36.10; Hobson et al. 2006, section 17.9), derived from linearized theory, plus the next order terms. For a point mass the energy-momentum tensor $T^{\mu\nu}$ contains a δ -function which allows easy evaluation of the integrals of the various moments to give

$$I^{jk} = c^2 \mu x_p^j x_p^k; \quad (29)$$

$$S^{ijk} = c \mu v_p^i x_p^j x_p^k; \quad (30)$$

$$M^{ijk} = c \mu x_p^i x_p^j x_p^k. \quad (31)$$

Since we are only interested in GWs, we shall use the transverse-traceless (TT) gauge. The waveform is given in the TT gauge by (Misner et al. 1973, box 35.1)

$$h_{jk}^{\text{TT}} = P_j^l h_{lm} P_k^m - \frac{1}{2} P_{jk} P^{lm} h_{lm}, \quad (32)$$

where the (spatial) projection operator P_{ij} is

$$P_{ij} = \delta_{ij} - n_i n_j. \quad (33)$$

4 DETECTION WITH LISA

The LISA detector is a three arm, space-borne laser interferometer (Bender et al. 1998; Danzmann & Rüdiger 2003). The three arms form an equilateral triangle that rotates as

[tbhp]

Figure 2. The relationship between the MBH's coordinate system x_\bullet^i and the SS coordinate system x_\odot^i . The MBH's spin axis is aligned with the z_\bullet -axis.

Figure 3. The relationship between the detector coordinates x_d^i and the ecliptic coordinates of the SS x_\odot^i (Bender et al. 1998).

the system's centre of mass follows a circular, heliocentric orbit, trailing 20° behind the Earth. To describe the detector configuration, and to transform from the MBH coordinate system to those of the detector, we will find it useful to define three coordinate systems: those of the BH at the GC x_\bullet^i , ecliptic coordinates centred at the solar system (SS) barycentre x_\odot^i , and coordinates that co-rotate with the detector x_d^i . The MBH's coordinate system and the SS coordinate system are depicted in Fig. 2. The currently envisioned LISA mission geometry is shown in Fig. 3. We define the detector coordinates such that the detector-arms lie in the x_d - y_d plane as shown in Fig. 4. The coordinate systems are related by a series of angles: Θ and Φ give the orientation of the SS in the MBH's coordinates. These define the orientation of the MBH's spin axis z_\bullet . $\bar{\Theta}$ and $\bar{\Phi}$ give the position of the GC in ecliptic coordinates. The angle Ψ specifies the relative inclinations of the z -axes of the SS and MBH: their orientation in the plane of the sky. $\bar{\phi}$ gives LISA's orbital phase and φ gives the rotational phase of the detector arms. Both of these vary linearly with time

$$\bar{\phi}(t) = \omega_\oplus t + \bar{\phi}_0; \quad \varphi(t) = -\omega_\oplus t + \varphi_0; \quad (34)$$

where ω_\oplus corresponds to one rotation per year. Finally, $\alpha = 60^\circ$ is the inclination of the detector plane. We have computed the waveforms in the MBH's coordinates, however it is simplest to describe the measured signal using the detector's coordinates.

The strains measured in the three arms can be combined such that LISA behaves as a pair of 90° interferometers at 45° to each other, with signals scaled by $\sqrt{3}/2$ (Cutler 1998). We will denote the two detectors as I and II. If we label the change in the three arms' lengths caused by GWs δL_1 , δL_2 and δL_3 , and use L for the unperturbed length, then detector I measures strain

$$h_{\text{I}}(t) = \frac{\delta L_1 - \delta L_2}{L} = \frac{\sqrt{3}}{2} \left(\frac{1}{2} h_d^{xx} - \frac{1}{2} h_d^{yy} \right), \quad (35)$$

and detector II measures

$$h_{\text{II}}(t) = \frac{\delta L_1 + \delta L_2 - 2\delta L_3}{\sqrt{3}L} = \frac{\sqrt{3}}{2} \left(\frac{1}{2} h_d^{xy} + \frac{1}{2} h_d^{yx} \right). \quad (36)$$

We will use vector notation $\mathbf{h}(t) = (h_{\text{I}}(t), h_{\text{II}}(t)) = \{h_A(t)\}$ to represent signals from both detectors.

Figure 4. The alignment of the three detector arms, with lengths L_1 , L_2 and L_3 , within the x_d - y_d plane (Cutler 1998). The origin of the detector coordinates coincides with the centre of mass of the constellation of satellites.

The final consideration for calculating the signal measured by LISA is the time of arrival of the signal: LISA's orbital position changes with time. Fortunately over the timescales of interest for parabolic encounters, these changes are small. We will assume that the position of the SS barycentre relative to the GC is constant: it is defined by the distance R_0 and the angles $\bar{\Theta}$ and $\bar{\Phi}$. The time of arrival at the SS barycentre t_\odot is then the retarded time; the time of detection t_d to lowest order is

$$t_d \simeq t_\odot - t_{\text{AU}} \cos [\bar{\phi}(t_\odot) - \bar{\Phi}] \sin \bar{\Theta}, \quad (37)$$

where t_{AU} is the light travel-time for LISA's orbital radius. The time t_d is required for $\phi(t)$ and $\varphi(t)$.

5 SIGNAL ANALYSIS

5.1 Frequency domain formalism

Having constructed the GW $\mathbf{h}(t)$ that will be incident upon the LISA detector, we may now consider how to analyse the waveform and extract the information it contains. We begin with a brief overview of the basic components of signal analysis used for GWs, with application to LISA in particular. This fixes notation. A more complete discussion of the material can be found in the work of Finn (1992), and Cutler & Flanagan (1994).

The measured strain $\mathbf{s}(t)$ will be the combination of the signal and the detector noise

$$\mathbf{s}(t) = \mathbf{h}(t) + \mathbf{n}(t); \quad (38)$$

we will assume that the noise $n_A(t)$ is stationary and Gaussian. When analysing signals, it is most convenient to work with the Fourier transform

$$\tilde{g}(f) = \mathcal{F}\{g(t)\} = \int_{-\infty}^{\infty} g(t) e^{2\pi i f t} dt. \quad (39)$$

For a Gaussian noise signal $n_A(t)$, each Fourier component $\tilde{n}_A(f)$ also has a Gaussian probability distribution; the assumption of stationarity means that different Fourier components are uncorrelated, thus (Cutler & Flanagan 1994)

$$\langle \tilde{n}_A(f) \tilde{n}_B^*(f') \rangle_n = \frac{1}{2} \delta(f - f') S_{AB}(f), \quad (40)$$

where $\langle \dots \rangle_n$ denotes the expectation value over the noise distribution, and $S_{AB}(f)$ is the (single-sided) noise spectral density. For simplicity, we may assume that the noise in the two detectors is uncorrelated, but share the same characterization so that (Cutler 1998)

$$S_{AB}(f) = S_n(f) \delta_{AB}. \quad (41)$$

The functional form of the noise spectral density $S_n(f)$ for LISA is discussed in Sec. 5.2.

The properties of the noise allow us to define a natural inner product and associated distance on the space of signals (Cutler & Flanagan 1994)

$$(g|\mathbf{k}) = 2 \int_0^\infty \frac{\tilde{g}_A^*(f) \tilde{k}_A(f) + \tilde{g}_B^*(f) \tilde{k}_B(f)}{S_n(f)} df. \quad (42)$$

Using this definition, the signal-to-noise ratio (SNR) is approximately

$$\rho[\mathbf{h}] = (\mathbf{h}|\mathbf{h})^{1/2}. \quad (43)$$

Figure 5. Approximate noise curve for LISA (Barack & Cutler 2004). The solid line includes both instrumental and confusion noise, the dashed line shows only instrumental.

The probability of a particular realization of noise $\mathbf{n}(t) = \mathbf{n}_0(t)$ is

$$p(\mathbf{n}(t) = \mathbf{n}_0(t)) \propto \exp \left[-\frac{1}{2} (\mathbf{n}_0|\mathbf{n}_0) \right]. \quad (44)$$

If the incident waveform is given as $\mathbf{h}(t)$, the probability of measuring signal $\mathbf{s}(t)$ is

$$p(\mathbf{s}(t)|\mathbf{h}(t)) \propto \exp \left[-\frac{1}{2} (\mathbf{s} - \mathbf{h}|\mathbf{s} - \mathbf{h}) \right]. \quad (45)$$

5.2 LISA noise curve

LISA's noise has two sources: instrumental noise and confusion noise, primarily from white dwarf binaries. The latter may be divided into contributions from galactic and extragalactic binaries. In this work we use the noise model of Barack & Cutler (2004). The shape of the noise curve can be seen in Fig. 5. The instrumental noise dominates at both high and low frequencies. The confusion noise is important at intermediate frequencies, and is responsible for the cusp around $f = 10^{-3}$ Hz.

5.3 Window functions

There is one remaining complication regarding signal analysis: since we are Fourier transforming a finite signal we encounter spectral leakage; a contribution from large amplitude spectral components leaks into other components (sidelobes), obscuring and distorting the spectrum at these frequencies (Harris 1978). This is an inherent problem with finite signals; it will be as much of a problem when analysing signals from LISA as it is computing waveforms here. To mitigate, but unfortunately not eliminate, these effects, the time-domain signal can be multiplied by a window function. These are discussed in detail in Appendix A. We have adopted the Nuttall four-term window with continuous first derivative (Nuttall 1981) for the results presented here.

6 PARAMETER ESTIMATION AND WAVEFORMS

6.1 Model parameters

The shape of the waveform depends on a number of parameters: those defining the MBH; those defining the companion object on its orbit, and those defining the LISA detector. Let us define $\boldsymbol{\lambda} = \{\lambda^1, \lambda^2, \dots, \lambda^N\}$ as the set of N parameters which specify the GW. For our model the input parameters are:

- (1) The MBH's mass M_\bullet . This is currently well constrained by the observation of stellar orbits about Sgr A* (Ghez et al. 2008; Gillessen et al. 2009), with the best estimate being $M_\bullet = (4.31 \pm 0.36) \times 10^6 M_\odot$. However this depends upon the galactic centre distance R_0 being accurately

known. If the uncertainty in this is included $M_\bullet = (3.95 \pm 0.06)_{\text{stat}} \pm 0.18_{|R_0, \text{stat}} \pm 0.31_{|R_0, \text{sys}} \times 10^6 M_\odot (R_0/8 \text{ kpc})^{2.19}$, where the errors are statistical, independent of R_0 ; statistical from the determination of R_0 , and systematic from R_0 respectively.

(2) The spin parameter a . Naively this could be anywhere in the range $|a| < M_\bullet$, however it may be limited by the accretion history. Considering the torque from radiation emitted by an accretion disc and swallowed by the BH it may be argued that $|a| \lesssim 0.998 M_\bullet$ (Thorne 1974). If the MBH grew via a series of randomly orientated accretion events, then the spin parameter can be low, and we expect an average value $|a| \sim 0.1\text{--}0.3 M_\bullet$ (King & Pringle 2006; King et al. 2008). We will use the convention that a is positive, and will change the sense of rotation by flipping the z -axis.

(3) The polar angle Θ defining the propagation direction.

(4) The inclination angle Ψ . Since a is positive, this is in the range $[-\pi, \pi]$.

(5) The SS-GC distance R_0 . As for M_\bullet , this is constrained by stellar orbits, the best estimate being (Gillessen et al. 2009) $R_0 = 8.33 \pm 0.35 \text{ kpc}$.

(6, 7) The coordinates of the MBH from the SS barycentre $\bar{\Theta}$ and $\bar{\Phi}$. These may be taken as the coordinates of Sgr A*, as the radio source is expected to be within ten Schwarzschild radii of the MBH (Reid et al. 2003; Doeleman et al. 2008). At the epoch J2000.0 (Reid et al. 1999) $\bar{\Theta} = 95.607669^\circ$, $\bar{\Phi} = 266.851760^\circ$. This will change with time due to the rotation of the SS about the GC, the proper motion is about 6 mas yr^{-1} , mostly in the plane of the galaxy (Reid et al. 1999; Backer & Sramek 1999; Reid et al. 2003).

(8) The angular momentum of the orbit about the MBH's spin axis L_z .

(9) The Carter constant for the orbit Q .

(10) The mass of the orbiting particle μ . This will depend upon the type of object: whether it is a MS star, WD, NS or BH.

(11–13) The initial position of the particle (x_0, y_0, z_0) . For specific values of Q and L_z there is a definite upper limit on $|z_0|/\sqrt{x_0^2 + y_0^2}$ given by the size of θ_0 from (20).

(14, 15) The orbital position of the LISA satellites given by $\bar{\phi}$ and φ . We will assume that the initial positions are chosen such that $\bar{\phi} = 0$ when $\varphi = 0$ (Cutler 1998).

The azimuthal angle Φ is omitted, since it arbitrarily defines the orientation of the MBH's x - and y -axes. We shall define it to be zero without loss of generality. We have a 15-dimensional parameter space. However, for a given signal arrival time the orbital parameters of LISA will be known; we will not try to infer these.

6.2 Waveforms

Figures 6–10 show example waveforms to demonstrate some of the possible variations in the signal. All these assume $M_\bullet = 8.6 \times 10^{31} \text{ kg} \simeq 4.3 \times 10^6 M_\odot$, $R_0 = 8.33 \text{ kpc}$, $\bar{\Theta} = 95.607669^\circ$, $\bar{\Phi} = 266.851760^\circ$ and $\mu = 10^{31} \text{ kg} \simeq 5 M_\odot$; other parameters are specified in the captions. The orbits specified in figures 6, 7 and 9 all loop once about the MBH — they are the simplest zoom-whirl orbits. The others, including the orbit of Fig. ??, are simpler trajectories that are

Figure 6. Waveform for model parameters: $a = 0.5 M_\bullet$, $\Theta = \pi/3$, $L_z = 3.67 M_\bullet$, $Q = 0.409 M_\bullet^2$, $x_0 = 3.0 \times 10^{12} \text{ m}$, $y_0 = 4.0 \times 10^{12} \text{ m}$, $z_0 = 2.0 \times 10^{11} \text{ m}$. The periaapse distance is $r_p = 4.67 M_\bullet$, the SNR is $\rho = 8800$.

Figure 7. Waveform for model parameters: $a = 0.5 M_\bullet$, $\Theta = \pi/3$, $L_z = 5.22 M_\bullet$, $Q = 0.055 M_\bullet^2$, $x_0 = 3.5 \times 10^{12} \text{ m}$, $y_0 = 3.5 \times 10^{12} \text{ m}$, $z_0 = 1.0 \times 10^{11} \text{ m}$. The periaapse distance is $r_p = 11.77 M_\bullet$, the SNR is $\rho = 140$.

recognisable as parabolic in shape. There is a clear distinction between the two types of orbit, as the loops introduce higher frequency harmonics.

The plotted waveforms use the oblate-spheroidal coordinate system for the NK. Using spherical polars makes negligible difference: on the scale shown here the only discernible difference would be in the spikes of the high-frequency tail of the orbits with smaller periaapses, and even that is minor. We conclude that the choice of coordinates for the kludge approximation is unimportant, and shall continue using oblate-spheroidal coordinates for the rest of this work.

6.3 Inference and Fisher matrices

Having detected a GW signal $\mathbf{s}(t)$ we are interested in what we can learn about the source. We have an inference problem that can be solved by appropriate application of Bayes' Theorem (Jaynes 2003, chapter 4): the probability distribution for our parameters given that we have detected the signal $\mathbf{s}(t)$ is given by the posterior

$$p(\boldsymbol{\lambda}|\mathbf{s}(t)) = \frac{p(\mathbf{s}(t)|\boldsymbol{\lambda})p(\boldsymbol{\lambda})}{p(\mathbf{s}(t))}. \quad (46)$$

Here $p(\mathbf{s}(t)|\boldsymbol{\lambda})$ is the likelihood of the parameters, $p(\boldsymbol{\lambda})$ is the prior probability distribution for the parameters, and $p(\mathbf{s}(t)) = \int p(\mathbf{s}(t)|\boldsymbol{\lambda}) d^N \boldsymbol{\lambda}$ is, for our purposes, a normalising constant and may be ignored. The likelihood function depends upon the realization of noise. A particular set of parameters $\boldsymbol{\lambda}_0$ defines a waveform $\mathbf{h}_0(t) = \mathbf{h}(t; \boldsymbol{\lambda}_0)$, the probability that we observe signal $\mathbf{s}(t)$ for this GW is given by (45), so the likelihood is

$$p(\mathbf{s}(t)|\boldsymbol{\lambda}_0) \propto \exp \left[-\frac{1}{2} (\mathbf{s} - \mathbf{h}_0 | \mathbf{s} - \mathbf{h}_0) \right]. \quad (47)$$

If we were to define this as a probability distribution for the parameters $\boldsymbol{\lambda}$, then the modal values would be the maximum-likelihood parameters $\boldsymbol{\lambda}_{\text{ML}}$. The waveform $\mathbf{h}(t; \boldsymbol{\lambda}_{\text{ML}})$ would be the signal closest to $\mathbf{s}(t)$ in the space of all signals, where distance is defined using the inner product (42) (Cutler & Flanagan 1994).

Figure 8. Waveform for model parameters: $a = 0.2 M_\bullet$, $\Theta = \pi/2$, $L_z = 10.45 M_\bullet$, $Q = 2.18 M_\bullet^2$, $x_0 = 3.5 \times 10^{12} \text{ m}$, $y_0 = 3.5 \times 10^{12} \text{ m}$, $z_0 = 5.0 \times 10^{11} \text{ m}$. The periaapse distance is $r_p = 53.7 M_\bullet$, the SNR is $\rho = 2.2$.

Figure 9. Waveform for model parameters: $a = 0.7M_\bullet$, $\Theta = \pi/2$, $L_z = 5.22M_\bullet$, $Q = 21.8M_\bullet^2$, $x_0 = 2.8 \times 10^{12}$ m, $y_0 = 2.8 \times 10^{12}$ m, $z_0 = 3.0 \times 10^{12}$ m. The periaapse distance is $r_p = 22.7M_\bullet$, the SNR is $\rho = 44$.

Figure 10. Waveform for model parameters: $a = 0.7M_\bullet$, $\Theta = \pi/2$, $L_z = 15.7M_\bullet$, $Q = 84.6M_\bullet^2$, $x_0 = 1.0 \times 10^{12}$ m, $y_0 = 4.2 \times 10^{12}$ m, $z_0 = 1.0 \times 10^{12}$ m. The periaapse distance is $r_p = 148M_\bullet$, the SNR is $\rho = 0.18$.

In the limit of a high SNR, we may approximate this as (Vallisneri 2008)

$$p(\mathbf{s}(t)|\lambda_0) \propto \exp \left[-\frac{1}{2} (\partial_a \mathbf{h} | \partial_b \mathbf{h}) (\lambda^a - \langle \lambda^a \rangle_\ell) (\lambda^b - \langle \lambda^b \rangle_\ell) \right], \quad (48)$$

where the mean is defined as

$$\langle \lambda^a \rangle_\ell = \frac{\int \lambda^a p(\mathbf{s}(t)|\lambda) d^N \lambda}{\int p(\mathbf{s}(t)|\lambda) d^N \lambda}. \quad (49)$$

Using the high SNR limit, this is the maximum-likelihood value $\langle \lambda^a \rangle_\ell = \lambda_{\text{ML}}^a$. The quantity

$$\Gamma_{ab} = (\partial_a \mathbf{h} | \partial_b \mathbf{h}) \quad (50)$$

is the Fisher information matrix. It controls the variance of the likelihood distribution.

The form of the posterior distribution will depend upon the nature of the prior information. If we have an uninformative prior, such that $p(\lambda)$ is a constant, then the posterior distribution would be determined by the likelihood. In the high SNR limit, we would obtain a Gaussian with variance-covariance matrix

$$\Sigma = \Gamma^{-1}. \quad (51)$$

The Fisher information matrix gives the uncertainty associated with the estimated parameter values, in this case the maximum-likelihood values.

If the prior were to restrict the allowed range for a parameter, for example, as is the case for the spin a , then the posterior would be a truncated Gaussian, and Γ^{-1} may no longer represent the variance-covariance.

If the prior were approximately Gaussian with variance-covariance matrix Σ_0 , then the posterior would also be Gaussian.³ The posterior variance-covariance would be (Cutler & Flanagan 1994; Vallisneri 2008)

$$\Sigma = (\Gamma + \Sigma_0^{-1})^{-1}. \quad (52)$$

From this the inverse Fisher matrix Γ^{-1} is an upper bound on the size of the posterior covariance matrix.⁴

³ If we only know the typical value and spread of a parameter then a Gaussian is the maximum entropy prior (Jaynes 2003, section 7.11): the prior that is least informative given what we do know.

⁴ It may also be shown to be the Cramér-Rao bound on the error covariance of an unbiased estimator (Cutler & Flanagan 1994; Vallisneri 2008). Thus it represents the frequentist error: the lower

To understand what we can from parabolic encounters alone, we will look at the inverse Fisher matrix elements. If these are small then we expect we would be able to precisely determine a parameter, whereas if they are large we would not be able to learn much more than we already know from our prior.

6.4 Inverse Fisher matrices

Calculating the inverse Fisher matrix for example orbits, we find that there is a large degeneracy between the mass μ and the distance R_0 . This is because the primary role of both is determining the amplitude of the waveform in (25). This is the only place that μ appears. We cannot determine both from an extreme mass-ratio burst. Consequently, to obtain well-conditioned inverse Fisher matrices, it is necessary to use our prior for R_0 . Including this we obtain a well defined inverse.

There are a few general properties. The parameters M_\bullet and Θ always have relatively small variances. These parameters are crucial for defining the BH system: M_\bullet sets the scale for the system and Θ the orientation. If a were small, the spacetime would be almost spherically symmetric and we would expect a large variance for Θ . The angular momentum L_z also has a small variance, it is important for specifying the orbit; its partner Q , however, does not always have a small variance, in fact in some cases it has one of the largest. This appears to correlate with the sizes of the covariances of Q : the orbits with the smallest periaapses have relatively large covariances for the set of parameters $\{a, Q, z_0\}$, indicating that there is some degeneracy between these. In these cases Q has a much larger variance, as does z_0 . The initial coordinates x_0 , y_0 and z_0 typically have small variances, the exception being the aforementioned case for z_0 .

The parameters with the largest variances are $\bar{\Theta}$ and μ . The large variance of $\bar{\Theta}$ reflects the poor angular resolution of gravitational wave detectors; $\bar{\Phi}$ has a smaller variance as a change in azimuthal position changes the waveform observed in the two detector arms. The particle mass μ has a large variance since it only alters the amplitude of the spectrum and not its shape.

The variances are smaller for larger values of the SNR as is expected. We are able to get such good values from the orbits with small periaapses since they have both a high SNR and the distinctive structure of a zoom-whirl orbit.

From this preliminary look at a few example orbits, it appears that we should be able to infer the mass of the Kerr BH at the GC from an EMRB. We can gain information regarding the spin of the MBH if the orbit's periaapsis is sufficiently small — we could learn nothing from the orbit of Table ???. The Fisher matrix analysis suggests that we should be able to accurately infer the spin orientation; however it seems likely that there could be difficulties for small spin values. This will require further investigation. It seems unlikely that we will be able to improve upon our cur-

bound on the covariance for an unbiased parameter estimator λ_{est} calculated from an infinite set of experiments with the same signal $\mathbf{h}(t)$ but different realizations of the noise $\mathbf{n}(t)$.

rent best estimate for the position of the MBH, but this is already well constrained.

What is particularly exciting is the amount of information we could obtain from a single encounter, which may be all that we would have the opportunity to observe with LISA. Taking the results of Table ??, which are for an orbit of periaapsis $r_p = 52.7M_\bullet$, as an example, we could infer maximum-likelihood values $M_\bullet = (4.32 \pm 0.07) \times 10^6 M_\odot$, $a = (0.50 \pm 0.02)M_\bullet$, and $\Theta = (60.0 \pm 1.6)^\circ$. Here we have ignored uncertainty introduced by the error in R_0 which will increase the uncertainty; however, we have also only considered information from GWs and not considered additional information from our prior knowledge: combining these as in (52) would give a smaller posterior variance. While further work will be needed to be certain how much we could expect to learn from EMRBs, this is encouraging.

7 ENERGY SPECTRA

To check that the NK waveforms are sensible, we may compare the energy spectra calculated from these with those obtained from the classic treatment of Peters & Mathews (1963); Peters (1964). This calculates GW emission for Keplerian orbits in flat spacetime, assuming only quadrupole radiation. The spectrum produced should be similar to that obtained from the NK in weak fields, that is for orbits with a large periaapsis; however we do not expect an exact match because of the differing input physics and various approximations.

We do not intend to use the kludge waveforms to calculate an accurate energy flux: this would be inconsistent as we assume that the orbits do not evolve with time. We only calculate the energy flux as a sanity check; to confirm that the kludge approximation is consistent with other approaches.

7.1 Kludge spectrum

A gravitational wave in the TT gauge has an effective energy-momentum tensor (Misner et al. 1973, section 35.15)

$$T_{\mu\nu} = \frac{c^4}{32\pi G} \langle \partial_\mu h_{ij} \partial_\nu h^{ij} \rangle, \quad (53)$$

where $\langle \dots \rangle$ indicates averaging over several wavelengths or periods. The flux of energy through a sphere of radius $r = R$ is

$$\frac{dE}{dt} = \frac{c^3}{32\pi G} R^2 \int d\Omega \left\langle \frac{dh_{ij}}{dt} \frac{dh^{ij}}{dt} \right\rangle, \quad (54)$$

with $\int d\Omega$ representing integration over all solid angles. From (25) we see that the waves have a $1/r$ dependence; if we define

$$h_{ij} = \frac{H_{ij}}{r}, \quad (55)$$

we see that the flux is independent of R , as required for energy conservation,

$$\frac{dE}{dt} = \frac{c^3}{32\pi G} \int d\Omega \left\langle \frac{dH_{ij}}{dt} \frac{dH^{ij}}{dt} \right\rangle. \quad (56)$$

If we now integrate to find the total energy emitted we obtain

$$E = \frac{c^3}{32\pi G} \int d\Omega \int_{-\infty}^{\infty} dt \frac{dH_{ij}}{dt} \frac{dH^{ij}}{dt}. \quad (57)$$

Since we are considering all time, the localization of the energy is no longer of importance and it is unnecessary to average over several periods. Switching to Fourier representation $\tilde{H}_{ij}(f) = \mathcal{F}\{H_{ij}(t)\}$,

$$E = \frac{\pi c^3}{4G} \int d\Omega \int_0^\infty df f^2 \tilde{H}^{ij}(f) \tilde{H}_{ij}^*(f), \quad (58)$$

using the fact that the signal is real so $\tilde{H}_{ij}^*(f) = \tilde{H}_{ij}(-f)$. From this we identify the energy spectrum as

$$\frac{dE}{df} = \frac{\pi c^3}{4G} \int d\Omega f^2 \tilde{H}^{ij}(f) \tilde{H}_{ij}^*(f). \quad (59)$$

7.2 Peters and Mathews spectrum

To calculate the Peters and Mathews energy spectrum for a parabolic orbit, we use the limiting result of Turner (1977)

$$\begin{aligned} \frac{dE}{df} = \frac{4\pi^2}{5} \frac{G^3}{c^5} \frac{M_\bullet^2 \mu^2}{r_p^2} & \left\{ \left[\frac{8f^2}{f_c^2} B\left(\frac{f}{f_c}\right) - \frac{2f}{f_c} A\left(\frac{f}{f_c}\right) \right]^2 \right. \\ & \left. + \left(\frac{128f^4}{f_c^4} + \frac{4f^2}{3f_c^2} \right) \left[A\left(\frac{f}{f_c}\right) \right]^2 \right\}, \end{aligned} \quad (60)$$

where f_c is the orbital frequency of a circular orbit of radius equal to r_p ,

$$f_c = \frac{1}{2\pi} \sqrt{\frac{G(M_\bullet + \mu)}{r_p^3}}, \quad (61)$$

and functions $A(\tilde{f})$ and $B(\tilde{f})$ are defined in terms of Bessel functions. Their precise forms are (Berry & Gair 2010)

$$A(\tilde{f}) = \frac{1}{\pi} \sqrt{\frac{2}{3}} K_{1/3} \left(\frac{2^{3/2} \tilde{f}}{3} \right); \quad (62)$$

$$\begin{aligned} B(\tilde{f}) = \frac{1}{\sqrt{3}\pi} & \left[K_{-2/3} \left(\frac{2^{3/2} \tilde{f}}{3} \right) + K_{4/3} \left(\frac{2^{3/2} \tilde{f}}{3} \right) \right. \\ & \left. - \frac{1}{\sqrt{2}\tilde{f}} K_{1/3} \left(\frac{2^{3/2} \tilde{f}}{3} \right) \right], \end{aligned} \quad (63)$$

where $K_\nu(z)$ is a modified Bessel function of the second kind. This result should be accurate to $\sim 10\%$ for orbits with periaapse radii larger than $\sim 10r_s$, where r_s is the MBH's Schwarzschild radius (Berry & Gair 2010).

7.3 Comparison

Two energy spectra are plotted in Fig. 11 for orbits with a periaapsis of $r_p = 35.0r_s$. For consistency with the approximation of Peters and Mathews the NK waveform has been calculated using only the quadrupole formula. The two spectra appear to be in good agreement, showing the same general shape. The NK spectrum is more tightly peaked, but is always within a factor of 2 (ignoring the high-frequency tail).

We may also compare the total energy flux. For the orbit shown in Fig. 11 integrating the NK spectrum gives $E_{\text{NK}} = 5.936 \times 10^{36}$ J; the Peters and Mathews total energy is $E_{\text{PM}} = 5.747 \times 10^{36}$ J. The total energy flux from the kludge waveform is larger than the Peters and Mathews result. This behaviour has been seen before for high eccentricity orbits about a non-spinning BH (Gair et al. 2005). It

Figure 11. Energy spectra for a parabolic orbit of a $\mu = 10^{31}$ kg $\simeq 5M_{\odot}$ object about a $M_{\bullet} = 8.8 \times 10^{36}$ kg $\simeq 4.3 \times 10^6 M_{\odot}$ Schwarzschild MBH with $L_z = 12M_{\bullet}$ and $Q = 0$; the periaapse distance is $r_p = 69.9M_{\bullet}$. The spectra calculated from a the NK waveform is shown by the solid line and the Peters and Mathews flux is indicated by the dashed line. The NK waveform only uses the quadrupole formula.

Figure 12. Energy spectra for the same orbit as shown in Fig. 11. The spectra calculated from a the NK waveform is shown by the solid line and the Peters and Mathews flux is indicated by the dashed line. The NK waveform includes contributions from the current quadrupole and mass octopole as given by (25).

may be explained by considering the total amount of rotation for the different orbits: the Peters and Mathews spectrum assumes a Keplerian orbit, so the total rotation is 2π ; the orbit in Kerr geometry rotates more than this (the angle would be 2π in the limit of an infinite periaapse, whereas for a periaapse small enough that the orbit shows zoom-whirl behaviour, the total angle may be many times 2π). The greater rotation leads to increased emission of gravitational waves and a larger energy flux (Berry & Gair 2010). From the level of agreement we may be confident that the NK waveforms are a reasonable approximation.

Introducing the octopole moments makes a small change to the energy spectrum, as seen in Fig. 12. The peak of the spectrum is shifted to a slightly higher frequency, and the total energy radiated is increased to $E_{\text{NK}} = 6.202 \times 10^{36}$ J. At such radii the higher order terms only make a correction of the order of a few percent.

8 DISCUSSION

We have outlined an approximate method of generating gravitational waveforms for EMRBs originating at the GC. These assume that the orbit is parabolic and employs a numerical kludge approximation. The two coordinate schemes for a NK presented here yield almost indistinguishable results. The waveforms created appear to be consistent with results obtained using Peters and Mathews waveforms in the weak-field regime. The NK approach should be superior to that of Peters and Mathews in the strong-field regime as it uses exact geodesics of Kerr spacetime.

Using the NK waveforms we have conducted a trial investigation, using Fisher matrix analysis, into how accurately we could infer parameters of the galactic centre's MBH should such an EMRB be observed. Potentially, it is possible to determine very precisely the key parameters defining the MBH's mass and spin, if the orbit gets close enough to the black hole. Unfortunately it does not appear possible to infer the distance to the GC because of a large degeneracy with the compact object's mass.

Before we can quote results for how accurately we can determine the various parameters, we must consider the probability of each orbit. This work would build upon the earlier results of Rubbo et al. (2006) and Hopman et al. (2007), who only considered the probability for a signal to be

detectable. To calculate these probabilities it will be necessary to assume a particular dynamical model for the galactic centre so that we can define distributions for angular momenta L_z and Q , mass μ and initial position. It will also be necessary to consider on which orbits MS stars would survive without being tidally disrupted (Kobayashi et al. 2004). Once the distribution of orbit parameters is known, it will be possible to assign probabilities to being able to infer parameters to a level of accuracy, for example there may be a probability $p = 0.05$ of constraining M_{\bullet} to within 0.01% and a probability $p = 0.25$ of constraining M_{\bullet} to within 1%. This could be done using a Monte Carlo method to sample the distribution of orbits, and calculating the variance-covariance matrix for the inferred parameters for each sample orbit. We could extend the simple Fisher matrix analysis performed here to a full Bayesian analysis with the distributions for L_z , Q , μ , x_0 , y_0 and z_0 serving as priors. However this may be too computationally expensive to justify implementing. From our preliminary investigation, which uses an extremely restricted sample of parameter space, it appears that we can achieve good results from a single EMRB with periaapsis of $r_p = 50M_{\bullet}$. This translates to a distance of 10^{11} m or 10^{-5} pc, and therefore may be unlikely to occur within the lifetime of LISA.

Some consideration should also be given to methods of fitting a waveform to an observed signal. Given an input signal, what is the best algorithm for finding the optimal set of parameters to characterize the observed waveform? It is necessary to consider this to check if there are degenerate combinations of parameters that produce similar waveforms; if these are sufficiently distinct in parameter space we would not be aware of them by only considering the region immediately about the ML point. We do not intend to use NK waveforms to actually identify real GWs: more accurate methods should be employed for that; the point of this study would be to identify potential pitfalls that could be encountered when using accurate waveforms.

A natural continuation of this work would be to consider EMRBs from other MBHs. LISA should be able to detect EMRBs originating from the Virgo cluster (Rubbo et al. 2006), however the detectable rate may be only 10^{-4} yr $^{-1}$ per galaxy (Hopman et al. 2007). It would be interesting to check what we could expect to infer about MBHs in other galaxies from GWs.

REFERENCES

- Amaro-Seoane P., Gair J. R., Freitag M., Miller M. C., Mandel I., Cutler C. J., Babak S., 2007, *Classical and Quantum Gravity*, 24, R113
- Babak S., Fang H., Gair J., Glampedakis K., Hughes S., 2007, *Physical Review D*, 75, 024005
- Backer D. C., Sramek R. A., 1999, *The Astrophysical Journal*, 524, 805
- Barack L., Cutler C., 2004, *Physical Review D*, 69, 082005
- Bekenstein J. D., 1973, *The Astrophysical Journal*, 183, 657
- Bender P., Brilliet A., Ciufolini I., Cruise A. M., Cutler C., Danzmann K., 1998, Technical report, LISA Pre-Phase A Report. Max-Planck-Institut für Quantenoptik, Garching

Berry C. P. L., Gair J. R., 2010, *Physical Review D*, 82, 107501

Boyer R. H., Lindquist R. W., 1967, *Journal of Mathematical Physics*, 8, 265

Burko L. M., Khanna G., 2007, *EPL*, 78, 60005

Carter B., 1968, *Physical Review*, 174, 1559

Carter B., 1971, *Physical Review Letters*, 26, 331

Chandrasekhar S., 1998, *The Mathematical Theory of Black Holes*. Oxford Classic Texts in the Physical Sciences, Oxford University Press, Oxford

Cutler C., 1998, *Physical Review D*, 57, 7089

Cutler C., Flanagan E. E., 1994, *Physical Review D*, 49, 2658

Damour T., Iyer B. R., Sathyaprakash B. S., 2000, *Physical Review D*, 62, 084036

Danzmann K., Rüdiger A., 2003, *Classical and Quantum Gravity*, 20, S1

de Felice F., 1980, *Journal of Physics A: Mathematical and General*, 13, 1701

Doeleman S. S., Weintroub J., Rogers A. E. E., Plambeck R., Freund R., 2008, *Nature*, 455, 78

Drasco S., Hughes S., 2004, *Physical Review D*, 69, 044015

Finn L. S., 1992, *Physical Review D*, 46, 5236

Gair J. R., Kennefick D. J., Larson S. L., 2005, *Physical Review D*, 72, 084009

Ghez A. M., Salim S., Weinberg N. N., Lu J. R., Do T., Dunn J. K., Matthews K., Morris M. R., Yelda S., Becklin E. E., Kremenek T., Milosavljevic M., Naiman J., 2008, *The Astrophysical Journal*, 689, 1044

Gillessen S., Eisenhauer F., Trippe S., Alexander T., Genzel R., Martins F., Ott T., 2009, *The Astrophysical Journal*, 692, 1075

Glampedakis K., Kennefick D., 2002, *Physical Review D*, 66, 044002

Harris F., 1978, *Proceedings of the IEEE*, 66, 51

Hawking S. W., 1972, *Communications in Mathematical Physics*, 25, 152

Hobson M. P., Efstathiou G., Lasenby A., 2006, *General Relativity: An Introduction for Physicists*. Cambridge University Press, Cambridge

Hopman C., Freitag M., Larson S. L., 2007, *Monthly Notices of the Royal Astronomical Society*, 378, 129

Israel W., 1967, *Physical Review*, 164, 1776

Israel W., 1968, *Communications in Mathematical Physics*, 8, 245

Jaynes E. T., 2003, *Probability Theory: The Logic of Science*. Cambridge University Press, Cambridge

Kaiser J., Schafer R., 1980, *Acoustics, Speech and Signal Processing*, IEEE Transactions on, 28, 105

Kato Y., Miyoshi M., Takahashi R., Negoro H., Matsumoto R., 2010, *Monthly Notices of the Royal Astronomical Society: Letters*, 403, L74

Kerr R., 1963, *Physical Review Letters*, 11, 237

King A. R., Pringle J. E., 2006, *Monthly Notices of the Royal Astronomical Society: Letters*, 373, L90

King A. R., Pringle J. E., Hofmann J. A., 2008, *Monthly Notices of the Royal Astronomical Society*, 385, 1621

Kobayashi S., Laguna P., Phinney E. S., Meszaros P., 2004, *The Astrophysical Journal*, 615, 855

Lynden-Bell D., Rees M. J., 1971, *Monthly Notices of the Royal Astronomical Society*, 152, 461

McKechan D. J. A., Robinson C., Sathyaprakash B. S.,

[htbp]

Figure A1. Example spectra calculated using a rectangular window. The high-frequency tail is the result of spectral leakage. The input parameters are: $M_{\bullet} = 4.3 \times 10^6 M_{\odot}$, $a = 0.5 M_{\bullet}$, $\Theta = \pi/3$, $\Phi = 0$, $R_0 = 8.33$ kpc, $\bar{\Theta} = 95.607669^\circ$, $\bar{\Phi} = 266.851760^\circ$, $\bar{\phi}_0 = 0$, $\varphi_0 = 0$, $L_z = 10.44 M_{\bullet}^2$, $Q = 0.055 M_{\bullet}^2$, $\mu = 5 M_{\odot}$, $x_0 = 3.5 \times 10^{12}$ m, $y_0 = 3.0 \times 10^{12}$ m, $z_0 = 1.0 \times 10^{11}$ m; see Sec. 6.1 for a discussion of these parameters. The periaapse distance is $r_p = 52.7 M_{\bullet}$. The high-frequency tail is the result of spectral leakage. The level of the LISA noise curve is indicated by the dashed line. The calculated SNR is $\rho = 11$.

2010, *Classical and Quantum Gravity*, 27, 084020

Merritt D., Alexander T., Mikkola S., Will C. M., 2010, *Physical Review D*, 81, 062002

Misner C. W., Thorne K. S., Wheeler J. A., 1973, *Gravitation*. W. H. Freeman, New York

Nuttall A., 1981, *IEEE Transactions on Acoustics, Speech and Signal Processing*, 29, 84

Peters P. C., 1964, *Physical Review*, 136, B1224

Peters P. C., Mathews J., 1963, *Physical Review*, 131, 435

Press W., 1977, *Physical Review D*, 15, 965

Psaltis D., 2008, *Living Reviews in Relativity*, 11

Rees M. J., 1984, *Annual Review of Astronomy and Astrophysics*, 22, 471

Reid M. J., Menten K. M., Genzel R., Ott T., Schödel R., Brunthaler A., 2003, *Astronomische Nachrichten*, 324, 505

Reid M. J., Readhead A. C. S., Vermeulen R. C., Treuhaft R. N., 1999, *The Astrophysical Journal*, 524, 816

Robinson D., 1975, *Physical Review Letters*, 34, 905

Rosquist K., Bylund T., Samuelsson L., 2009, *International Journal of Modern Physics D*, 18, 429

Rubbo L. J., Holley-Bockelmann K., Finn L. S., 2006, *The Astrophysical Journal*, 649, L25

Ruffini R., Sasaki M., 1981, *Progress of Theoretical Physics*, 66, 1627

Thorne K. S., 1974, *The Astrophysical Journal*, 191, 507

Turner M., 1977, *The Astrophysical Journal*, 216, 610

Vallisneri M., 2008, *Physical Review D*, 77, 042001

Wilkins D., 1972, *Physical Review D*, 5, 814

APPENDIX A: WINDOW FUNCTIONS

When we perform a Fourier transform using a computer we must necessarily only transform a finite time-span τ . The effect of this is the same as transforming the true, infinite signal multiplied by a unit top-hat function of width equal to the time-span. Fourier transforming this yields the true waveform convolved with a sinc. If $\tilde{h}'(f)$ is the computed Fourier transform then

$$\tilde{h}'(f) = \int_{-\tau/2}^{\tau/2} h(t) e^{2\pi i f t} dt = [\tilde{h}(f) * \tau \text{sinc}(\pi f \tau)], \quad (\text{A1})$$

where $\tilde{h}(f) = \mathcal{F}\{h(t)\}$ is the unwindowed Fourier transform of the infinite signal. This windowing of the data is a problem inherent in the method and results in spectral leakage.

Figure A1 shows the computed Fourier transforms for an example parabolic encounter. The waveforms have two distinct regions: a low-frequency curve, and a high-frequency

tail. The low-frequency signal is the spectrum we are interested in; the high-frequency components are the result of spectral leakage. The $\mathcal{O}(1/f)$ behaviour of the sinc gives the shape of the tail. This has possibly been misidentified in figure 8 of Burko & Khanna (2007) as the characteristic strain for parabolic encounters.

Despite being many orders of magnitude below the peak level, the high-frequency tail is still well above the noise curve for a wide range of frequencies. It therefore contributes to the evaluation of any inner products, and could mask interesting features. It is possible to reduce the amount of leakage using apodization: to improve the frequency response of a finite time series one can use a weighting window function $w(t)$ which modifies the impulse response in a prescribed way. The simplest window function is the rectangular (or Dirichlet) window $w_R(t)$; this is just the top-hat described above. Other window functions are generally tapered.⁵ There is a wide range of window functions described in the literature (Harris 1978; Kaiser & Schafer 1980; Nuttall 1981; McKechan et al. 2010). The introduction of a window function influences the spectrum in a manner dependent upon its precise shape; there are two distinct distortions: local smearing due to the finite width of the centre lobe, and distant leakage due to finite amplitude sidelobes. The window function may be optimised such that the peak sidelobe has a small amplitude, or such that the sidelobes decay away rapidly with frequency. Choosing a window function is a trade-off between these various properties, and will depend upon the particular application.

For use with the parabolic spectra, the primary concern is suppress the sidelobes. Many windows with good sidelobe behaviour exist in the literature, we will consider three: the Blackman-Harris minimum four-term window (Harris 1978; Nuttall 1981)

$$w_{\text{BH}}(t) = \sum_{n=0}^3 a_n^{\text{BH}} \cos\left(\frac{2n\pi t}{\tau}\right), \quad (\text{A2})$$

where

$$\begin{aligned} a_0^{\text{BH}} &= 0.35875, & a_1^{\text{BH}} &= 0.48829, \\ a_2^{\text{BH}} &= 0.14128, & a_3^{\text{BH}} &= 0.01168; \end{aligned} \quad (\text{A3})$$

the Nuttall four-term window with continuous first derivative (Nuttall 1981)

$$w_{\text{N}}(t) = \sum_{n=0}^3 a_n^{\text{N}} \cos\left(\frac{2n\pi t}{\tau}\right), \quad (\text{A4})$$

where

$$\begin{aligned} a_0^{\text{N}} &= 0.355768, & a_1^{\text{N}} &= 0.487396, \\ a_2^{\text{N}} &= 0.144232, & a_3^{\text{N}} &= 0.012604; \end{aligned} \quad (\text{A5})$$

and the Kaiser-Bessel window (Harris 1978; Kaiser & Schafer 1980)

$$w_{\text{KB}}(t; \beta) = \frac{I_0\left[\beta\sqrt{1-(2t/\tau)^2}\right]}{I_0(\beta)}, \quad (\text{A6})$$

⁵ When using a tapered window function it is important to ensure that the window is centred upon the signal; otherwise the calculated transform will have a reduced amplitude.

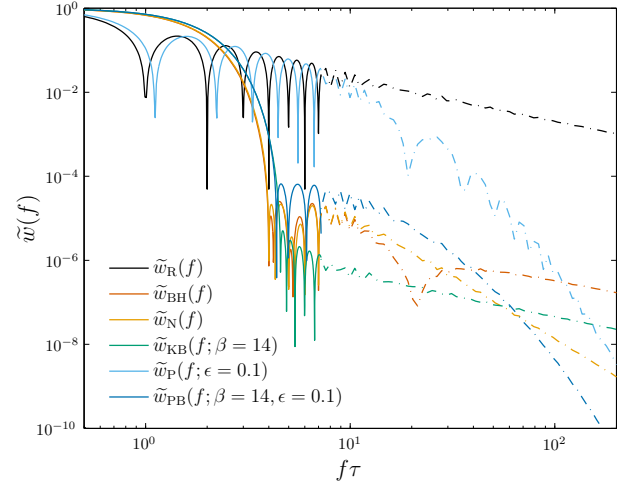


Figure A2. Window function frequency response. To avoid clutter, the response function is only plotted in detail until $f\tau = 8$, above this a smoothed value is plotted, as indicated by the dot-dashed line. As well as having good asymptotic behaviour, the Planck-taper window has the narrowest main lobe, except for the rectangular window.

where $I_\nu(z)$ is the modified Bessel function of the first kind, and β is an adjustable parameter. The Kaiser-Bessel window has the smallest peak sidelobe, but the worst decay ($1/f$); the Nuttall window has the best asymptotic behaviour ($1/f^3$); the Blackman-Harris window has a peak sidelobe similar to the Nuttall window, and decays asymptotically as fast (slow) as the Kaiser-Bessel window, but has the advantage of having suppressed sidelobes next to the central lobe. Another window has been recently suggested for use with gravitational waveforms: the Planck-taper window (Damour et al. 2000; McKechan et al. 2010)

$$w_{\text{P}}(t; \epsilon) = \begin{cases} \frac{1}{\exp(Z_+) + 1} & -\frac{\tau}{2} \leq t < -\tau\left(\frac{1}{2} - \epsilon\right) \\ 1 & -\tau\left(\frac{1}{2} - \epsilon\right) < t < \tau\left(\frac{1}{2} - \epsilon\right) \\ \frac{1}{\exp(Z_-) + 1} & -\tau\left(\frac{1}{2} - \epsilon\right) < t \leq \frac{\tau}{2} \end{cases}, \quad (\text{A7})$$

with

$$Z_{\pm}(t; \epsilon) = 2\epsilon \left[\frac{1}{1 \pm 2(t/\tau)} + \frac{1}{1 - 2\epsilon \pm 2(t/\tau)} \right]. \quad (\text{A8})$$

This was put forward for use with binary coalescences, and has superb asymptotic decay. However, the peak sidelobe is high, which could be disadvantages for this application. We therefore propose a new window function: the Planck-Bessel window which simply combines the Kaiser-Bessel and Planck-taper windows to produce a window which inherits the best features of both, albeit in a diluted form

$$w_{\text{PB}}(t; \beta, \epsilon) = w_{\text{P}}(t; \epsilon) w_{\text{KB}}(t; \beta). \quad (\text{A9})$$

The window functions' frequency responses are plotted in Fig. A2. There is no window that performs best everywhere.

Figure A3 shows the computed Fourier transforms for an example parabolic encounter using no window (alternatively a rectangular or Dirichlet window), and the

[htbp]

Figure A3. Example spectra calculated using (a) a rectangular window and (b) Nuttall’s four-term window with continuous first derivative (Nuttall 1981). The input parameters are: $M_\bullet = 3.3 \times 10^6 M_\odot$, $a = 0.5 M_\bullet$, $\Theta = \pi/3$, $\Phi = 0$, $R_0 = 8.33$ kpc, $\bar{\Theta} = 95.607669^\circ$, $\bar{\Phi} = 266.851760^\circ$, $\bar{\phi}_0 = 0$, $\varphi_0 = 0$, $L_z = 10.44 M_\bullet$, $Q = 0.055 M_\bullet^2$, $\mu = 5 M_\odot$, $x_0 = 3.5 \times 10^{12}$ m, $y_0 = 3.0 \times 10^{12}$ m, $z_0 = 1.0 \times 10^{11}$ m; see Sec. 6.1 for a discussion of these parameters. The periaapse distance is $r_p = 52.7 M_\bullet$. The high-frequency tail is the result of spectral leakage. The level of the LISA noise curve is indicated by the dashed line. The spectra are from detector I, detector II has similar spectra.

Nuttall four-term window with continuous first derivative (Nuttall 1981).⁶ The waveforms have two distinct regions: a low-frequency curve, and a high-frequency tail. The low-frequency signal is the spectrum we are interested in; the high-frequency components are the result of spectral leakage. Using the Nuttall window, the spectral leakage is greatly reduced; the peak sidelobe is lower, and the tail decays away as $1/f^3$ instead of $1/f$.

The choice of window function will influence the results as it changes the form of $\tilde{h}(f)$. The variation in results between windows depends upon the signal: variation is greatest for low frequency bursts, as then there is greatest scope for leakage into the LISA frequency band; variation is least significant for zoom-whirl orbits as then there are strong signals to relatively high frequencies, and spectral leakage is confined to mostly below the noise level. To quantify the influence of window functions, we studied the diagonal elements of the Fisher matrix from a selection of orbits with periaapses ranging from $\sim 10 M_\bullet$ – $300 M_\bullet$. For orbits with small periaapses all five windows (excluding the rectangular window) produced very similar results: the Planck-taper window differed by a maximum of $\sim 0.5\%$ from the others, which all agreed to better than 0.1% . The worst case results came from the lowest frequency orbits, then the Planck-taper window deviated by a maximum of $\sim 30\%$ in the value for the Fisher matrix elements, the Blackman-Harris deviated by $\sim 20\%$ and the others agreed to better than $\sim 5\%$. The Planck-taper window’s performance is limited by its poor sidelobe behaviour; the Blackman-Harris has the worst performance at high frequency.

For this work we have used the Nuttall window. Its performance is comparable to the Kaiser-Bessel and Planck-Bessel windows, however it is computationally less expensive to implement as it does not contain Bessel functions. Results should be accurate to a few percent at worst, and results from closer orbits, which provide better constraints, should be less affected by the choice of window function. Therefore, we are confident that none of our conclusions are sensitive to the particular windowing method implemented.

This paper has been typeset from a \LaTeX file prepared by the author.

⁶ The Blackman-Harris minimum four-term window (Harris 1978; Nuttall 1981), and the Kaiser-Bessel window (Harris 1978; Kaiser & Schafer 1980) give almost identical results.